Reliable k·p band structure calculation for nanostructures using finite elements

**Ratko G. Veprek · Sebastian Steiger ·
Bernd Witzigmann**

Abstract The **k·p** envelope function method is a popular tool for the study of electronic properties of III–V nanostructures. The equations are usually transferred to real-space and solved using standard numerical techniques. The powerful and flexible finite element method was seldom employed due to problems with spurious solutions. The method would be favorable for the calculation of electronic properties of large strained nanostructures as it allows a flexible representation of complex geometries. In this paper, we show our consistent implementation of the **k·p** envelope equations for nanostructures of any dimensionality. By including Burt-Foreman operator ordering and ensuring the ellipticity of the equations, we are able to calculate reliable and spurious solution free subband structures for the standard **k·p** 4×4, 6×6 and 8 × 8 models for zinc-blende and wurtzite crystals. We further show how to consistently include strain effects up to second order by means of the Pikus-Bir transformation. Finally, we analyze the performance of our implementation using benchmark examples.

Keywords Nanostructures · **k·p** · Strain · Finite elements · Bandstructure · Spurious solutions

1 Introduction

With the advent of quantum-sized optoelectronic devices such as quantum dot, wire and well light emitting diodes

R.G. Veprek (✉) · S. Steiger · B. Witzigmann
Integrated Systems Laboratory, Department of Information Technology and Electrical Engineering, ETH Zurich, Gloriastrasse 35, 8092 Zurich, Switzerland
e-mail: veprek@iis.ee.ethz.ch

and lasers, computer simulation demands accurate, fast and reliable prediction of the electronic band structure of III–V and nitride semiconductors. Atomistic methods, such as the empirical tight-binding, pseudopotential or density functional method using a repeated super-cell formulation, allow to describe the electronic properties to a high precision. Unfortunately the extreme demand in computational resources restricts their application in device-design to small and simple systems. In contrast, the **k·p** envelope function method can be formulated as a partial differential equation system and therefore allows to determine the band structure efficiently using standard numerical techniques. Various simplifications during the perturbative treatment of remote bands obfuscate physical details, such as intervalley- and interface mixing [1, 2]. This leads to an ongoing dispute about the precision and validity of the obtained results [3–6] where the raised arguments apply to the commonly used **k·p** standard model. It was shown recently [1, 2] that an exact derivation of the envelope equations from first principles does allow for a consistent incorporation of interface mixing effects and an exact description of the band structure.

Nevertheless, due to its usually sufficient accuracy and simplicity, the standard **k·p** model is widely used in academia and industry for the determination of band structures in quantum wells and less frequently for wires and dots.

A major obstacle in the application and reliability of the **k·p** method is the appearance of spurious solutions that are highly oscillatory, produce energy bands bending into the wrong direction and sometimes lead to unphysical solutions extending into the forbidden bandgap. The finite element (FE) method suffers especially severely from these solutions which might explain its rare application. As demonstrated in [7], the spurious solutions go hand in hand with the lack of ellipticity of the envelope equations. The ellipticity can be

recovered using Burt-Foreman (BF) operator ordering [8–10] and a careful choice of input parameters (compare with eqn. (30) in [7]). The elliptic formulation of the envelope equations allows us to reliably apply the FE method without occurrence of spurious solutions.

The FE method has advantages over other methods such as the finite difference (FD) method as it allows modelling of complex geometries defined on non-tensorial grids without staircase surfaces. The major difference however is that the FE method describes an approximation to the solution while the FD method is an approximation of the equations. The FD method needs a careful mixture of forward- and backward differences to guarantee the hermiticity and numerical stability of the equation system [11].

The aim of this paper is to present a consistent FE formulation of the envelope equations for nanostructures of any dimension that we have implemented in a C++ computer program named *tdkp*. Using BF operator ordering, elliptic envelope equations, parallel programming, sparse matrix- and iterative solver techniques, our solver is able to deliver fast, accurate and reliable band structure results. We implemented 4×4, 6×6 and 8×8 models for zinc-blende and 6×6 and 8×8 models for wurtzite crystals. Strain effects are treated using continuum equations and their effects on the band structure are consistently included up to second order.

2 Envelope equations

The envelope equations of the standard $\mathbf{k} \cdot \mathbf{p}$ model consist of a coupled set of partial differential equations up to second order, defined by the eigenequation of the $\mathbf{k} \cdot \mathbf{p}$ differential operator

$$
\begin{aligned}
\mathbf{H_{kp}} = &-\sum_{i,j} \partial_i \mathbf{H}_{ij}^{(2)}(\mathbf{x}; \mathbf{k}_t) \partial_j \\
&+ \sum_i \left(\mathbf{H}_{i;L}^{(1)}(\mathbf{x}; \mathbf{k}_t) \partial_i + \partial_i \mathbf{H}_{i;R}^{(1)}(\mathbf{x}; \mathbf{k}_t) \right) \\
&+ \mathbf{H}^{(0)}(\mathbf{x}; \mathbf{k}_t).
\end{aligned} \tag{1}
$$

Indices over i and j denote the quantized directions and the equation is parametrized in terms of the transverse wavenumber $\mathbf{k}_t$. The details of the $\mathbf{k} \cdot \mathbf{p}$ model such as the BF operator ordering, the considered number of bands, the basis choice and the crystal type determines the form of the parametric $\mathbf{k} \cdot \mathbf{p}$ matrices $\mathbf{H}_.^{(.)}(.)$. Other second order operators such as

$$
\partial_i \partial_j \mathbf{H} \quad \text{and} \quad \mathbf{H} \partial_i \partial_j \tag{2}
$$

do not appear in the standard $\mathbf{k} \cdot \mathbf{p}$ model but exist in the first-principles model of [1]. According to the dimensional-

ity of the considered system, bulk second-order terms depending on the translationally invariant direction are effectively added to first and zero order terms of the differential operator:

$$
\begin{aligned}
\partial_i \mathbf{H}_{it}^{(2)} k_t &\rightarrow \partial_i \mathbf{H}_{i;R}^{(1)} \\
k_t \mathbf{H}_{ti}^{(2)} \partial_i &\rightarrow \mathbf{H}_{i;L}^{(1)} \partial_i \\
k_t \mathbf{H}_{tt}^{(2)} k_t &\rightarrow \mathbf{H}^{(0)}.
\end{aligned} \tag{3}
$$

The usual approach of constructing the envelope equations from bulk $\mathbf{k} \cdot \mathbf{p}$ Hamiltonians is to replace the wavenumbers $\mathbf{k}_q$ of the symmetry broken directions with the corresponding operators $-i \nabla_q$. This particular approach cannot be applied, as in the bulk Hamiltonian the ordering of a second order term $\mathbf{H} k_i k_j$ is lost. Therefore, the distribution into

$$
k_i \mathbf{H}_+ k_j + k_j \mathbf{H}_- k_i \tag{4}
$$

is unknown. A naive symmetric distribution between these terms leads to a non-elliptic equation system which results in spurious solutions [7]. In contrast, the BF operator ordering results in an asymmetric distribution between $\mathbf{H}_+$ and $\mathbf{H}_-$ preserving ellipticity [8–10].

The effect of symmetry breaking in arbitrary crystal planes can be calculated by an appropriate rotation of the real space system into principal directions.

2.1 Zinc-blende models

To describe III–V semiconductors with zinc-blende crystal structure, we consider four different models. The simplest model is the one-band effective mass that also easily fits into the given equation frame but will not be discussed any further. The $\mathbf{k} \cdot \mathbf{p}$ 4×4 model describes the Γ_8 valence band (light- and heavy hole), the 6×6 model adds the Γ_7 split-off band, and the 8×8 model further includes the Γ_6 conduction band. Usual $\mathbf{k} \cdot \mathbf{p}$ implementations [12–19] are based on model Hamiltonians expressed in terms of the diagonal Bloch basis at the Γ point. We found it more convenient to use the Pidgeon-Brown or Enders Hamiltonian [20, 21] given in the zone-center basis

$$
S\uparrow, \ X\uparrow, \ Y\uparrow, \ Z\uparrow, \ S\downarrow, \ X\downarrow, \ Y\downarrow, \ Z\downarrow \tag{5}
$$

for which the spin orbit terms are non-diagonal at $k = 0$. The reason for our choice is that the BF operator ordering keeps a simple and clear form (see eqn. (11) in [10]) in that particular basis. All diagonal terms are treated in the standard way $M k_x^2 \rightarrow k_x M k_x$ while the offdiagonal terms $N k_i k_j$ in the valence band are split asymmetrically

$$
N k_i k_j \rightarrow k_i N_+ k_j + k_j N_- k_i \tag{6}
$$

and N_- is estimated as [10]

$$N_- = M - \frac{\hbar^2}{2m_0}. \tag{7}$$

The first order terms in the 8×8 model also require some care: The self-adjoint of the first order term iPk_j is given by $-ik_j P$. Wrong operator ordering there leads to a non-hermitian equation system. The explicit form of the 8×8 Hamiltonian is given in [7, 10, 20, 21]. The 6×6 Hamiltonian is obtained from the 8×8 model by taking the limit $E_g \to \infty$ and neglecting the Γ_6 conduction band. In order to obtain the 4×4 Hamiltonian, one performs a basis transformation diagonalizing the 6×6 Hamiltonian at $k = 0$ and then neglects the Γ_7 split-off band. By keeping track of the ordered terms of eqn. (6), the Burt-Foreman operator ordering is transfered into 4×4 model terms having again the form $k_i A_n k_j - k_j A_n k_i$ [22].

2.2 Wurtzite models

With the advent of blue lasers and LEDs, wurtzite nitride semiconductors have recently drawn high attention. We have implemented the $\mathbf{k} \cdot \mathbf{p}$ 6×6 model for the valence bands derived by Chuang [23] and it's extension to the 8×8 model [24] including the conduction band. The BF operator ordering for this model has been derived by Mireles et al. [25] and leads to results similar to the zinc-blende case. The relevant unsymmetrical BF splitting of the parameters affects the off-diagonal terms N_1 and N_2 which, again using the zone center basis, split into

$$N_1 k_x k_y \to k_x N_{1+} k_y + k_x N_{1-} k_y. \tag{8}$$

These parameters are related to the more commonly used A_i effective mass parameters [23] by

$$\frac{\hbar^2}{2m_0} A_5 = \frac{N_1}{2}, \qquad \frac{\hbar^2}{2m_0} A_6 = \frac{N_2}{\sqrt{2}}. \tag{9}$$

The detailed distribution between N_{1+}, N_{1-} and N_{2+}, N_{2-} in terms of the A_i parameters has been given in [25, 26]. As the N_{i-} have contributions only from a remote d-like conduction band, they are believed to be small compared to N_{i+} [25]. This suggestion is supported using the ellipticity analysis of the envelope equation system [7]. In Fig. 1, we use the measure ρ suggested in eqn. (31) of [7] to visualize the degree of non-ellipticity of the equation system depending on the splitting of A_5 and A_6 so that

$$A_i = A_{i+} + A_{i-} \tag{10}$$

and plot iso-lines for the non-ellipticity ratio depending on the choices of A_{i+}. The equation system is elliptic if $\rho = 0$. The figure shows the situation for InN material parameters
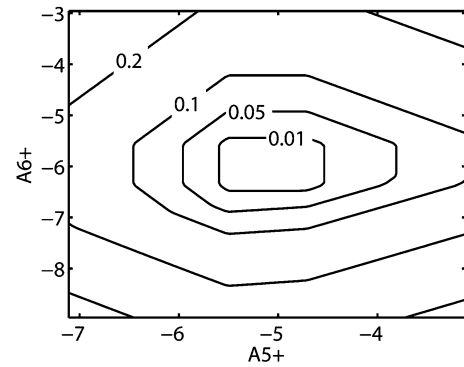

Fig. 1 Non-ellipticity analysis for parameter splitting A_{i+} and A_{i-} in InN for fixed parameters $A_5 = -5.11$ and $A_6 = -5.96$ [27]. The completely asymmetric splitting leads to elliptic equation systems

($A_5 = -5.11$ and $A_6 = -5.96$) taken from [27] but similar results also apply to GaN and AlN. The equation system is elliptic only for the nearly complete asymmetric splitting. The asymmetric splitting of [25] applied to nitride parameters given by [27] leads to smaller, but still nonzero values for ρ and therefore to non-elliptic equations. Therefore, we usually follow the ellipticity criterion and set

$$A_{i-} = 0. \tag{11}$$

3 Strain effects

3.1 Continuum elasticity

The different lattice constants of semiconductors can lead to high internal strains, which substantially modify the electronic properties. While the strain in biaxially strained quantum wells can be calculated analytically, strains in complex geometries of wires and dots require numerical determination [12, 13, 15, 17, 18, 28]. In order to be consistent with the continuum approach of the envelope method, we apply small strain-linear continuum elasticity. Here, the elastic strain tensor ε_{ij} is defined in terms of the displacement vector $\mathbf{u}$ as

$$\varepsilon_{ij} = \frac{1}{2} \left(\frac{\partial u_i}{\partial x_j} + \frac{\partial u_j}{\partial x_i} \right). \tag{12}$$

The strains in certain material systems can be very large leading to a misdescription of the strain field [29]. A correct description of large strains in terms of continuum elasticity would require the use of non-linear large strain analysis.

The elastic strain energy of the system is given by

$$\Pi = \int \frac{1}{2} \sum_{ij} \sigma_{ij} \varepsilon_{ij} \, d\Omega. \tag{13}$$

Here σ_{ij} denotes the stress tensor which is related to the strain via the elastic coefficient matrix $\mathbf{C}$ [19]. As bulk zinc-blende materials are cubic, the number of independent elastic coefficient elements is reduced to three independent constants, C_{11}, C_{12} and C_{44}. In wurtzite crystals, the elastic response is different along c- and a-axis, leading to additional elastic coefficients C_{13}, C_{33} and C_{66}.

In order to include the intrinsic strain of a quantized region, the system is regarded as a shrink-fit problem. The system is assumed to be embedded within a host material with a reference lattice constants $a_{r,i}$. This leads to a position dependent intrinsic strain given by

$$\varepsilon_{ii}^0(\mathbf{x}) = \frac{a_{r,i} - a_{q,i}(\mathbf{x})}{a_{q,i}(\mathbf{x})} \tag{14}$$

which is added to the strain in (13). $a_{q,i}(\mathbf{x})$ denotes the position dependent lattice constant of the crystal. In zinc-blende crystals, the lattice constant is isotropic, while wurtzite crystals have different lattice constants for the c- and the a-axis. The relaxed configuration is then obtained by finding the displacement field $\mathbf{u}$ minimizing the energy given by (13).

3.2 Strains in $\mathbf{k}\cdot\mathbf{p}$ theory

The strained $\mathbf{k}\cdot\mathbf{p}$ Hamiltonian can be obtained from the Hamiltonian without strain by means of the Pikus-Bir transformation where the strained system is mapped to the unstrained crystal. The strain-dependent Hamiltonian can be obtained from the unstrained $\mathbf{H}_0$ by [21, 30]

$$\mathbf{H}_\varepsilon(\boldsymbol{\varepsilon}, \mathbf{k}) = \mathbf{H}_0((\mathbf{1} - \boldsymbol{\varepsilon})\mathbf{k}) + \mathbf{D}(\boldsymbol{\varepsilon}), \tag{15}$$

where $\mathbf{D}(\boldsymbol{\varepsilon})$ is the deformation potential contribution [31]. The Hamiltonian in the form of (15) is particularly elegant and suited for numerical implementation as for example second order terms are simply transformed to

$$\mathbf{H}_{\varepsilon,ij}^{(2)} = \sum_{mn}(\mathbf{1} - \boldsymbol{\varepsilon})_{im}^T \mathbf{H}_{mn}^{(2)}(\mathbf{1} - \boldsymbol{\varepsilon})_{nj} \tag{16}$$

and $\mathbf{D}(\boldsymbol{\varepsilon})$ can be added to the zero order terms. Thereby, strain effects are consistently included in the equation system up to second order, which obviates the inclusion of explicitly strain dependent effective masses.

4 Numerical formulation and determination

4.1 Envelope equations

Using the $\mathbf{k}\cdot\mathbf{p}$ differential operator $\mathbf{H}_{\mathbf{kp}}$, the envelope equation to solve is given by

$$\mathbf{H}_{\mathbf{kp}}\mathbf{F}(\mathbf{x}) = E\,\mathbf{F}(\mathbf{x}), \tag{17}$$

where $\mathbf{F}(\mathbf{x})$ is the envelope vector describing at each position of the nanostructure how the bulk Bloch states are mixed. Usually either a spectral or the FD method is applied. For the FE method, several derivations for different dimensionalities exist [32–34]. Here, we focus on a general form that is applicable to wells, wires and dots for any $\mathbf{k}\cdot\mathbf{p}$ model. Therefore, we cast (17) into a weak form and apply the FE discretization.

Let Ω be the volume of interest with boundary $\partial\Omega$ and let H^1 be the Sobolev space with square-integrable weak derivatives [35] up to order 1, which we use as the space for the relevant envelope functions $F_i(\mathbf{x})$. As we are merely interested in bound states, we use Dirichlet boundary conditions at the volume boundary and therefore define the solution space to be

$$V = \left\{ u \in H^1 : u(\partial\Omega) = 0 \right\}. \tag{18}$$

The variational form of the envelope equation (17) is obtained by multiplying with a test function $\mathbf{W}(\mathbf{x}) \in V$ and integrating over Ω, leading to

$$\int_\Omega \sum_{ij} \partial_i \mathbf{W}^\star \mathbf{H}_{ij}^{(2)} \partial_j \mathbf{F}\, d\mathbf{x}$$

$$+ \int_\Omega \sum_i \mathbf{W}^\star \mathbf{H}_{i;L}^{(1)} \partial_i \mathbf{F} - \partial_i \mathbf{W}^\star \mathbf{H}_{i;R}^{(1)} \mathbf{F}\, d\mathbf{x} \tag{19}$$

$$+ \int_\Omega \mathbf{W}^\star \mathbf{H}^{(0)} \mathbf{F} = E \int_\Omega \mathbf{W}^\star \mathbf{F}\, d\mathbf{x}.$$

In (19), the first integral and the second part of the second integral were partially integrated using the Dirichlet boundary conditions of (18). Thus, the singularity of $\partial_i \mathbf{H}_{i;R}^{(1)}$ at the material interface is removed and no complicated tweaks in the numerical evaluation have to be applied. Let $a(\mathbf{W}, \mathbf{F})$ denote the left-hand side bilinear form and $(\mathbf{W}, \mathbf{F})_0$ the right-hand side bilinear form of (19). The generalized solutions of (17) are defined as $(\hat{\lambda}_n, \hat{\mathbf{F}}_n)$ $(\hat{\mathbf{F}}_n \in V)$ where

$$a(\mathbf{W}, \hat{\mathbf{F}}_n) = \hat{\lambda}_n (\mathbf{W}, \hat{\mathbf{F}}_n)_0 \quad \forall \mathbf{W} \in V. \tag{20}$$

There is no need to explicitly enforce special boundary conditions inside Ω at a given material interface. Such boundary conditions are implicitly included in the given differential operator and are denoted in the finite element framework as *natural boundary conditions*.

To solve (20) numerically, it must first be converted into an algebraic equation of finite size. Therefore let

$$V_M \subset V \tag{21}$$

be a linear subspace of V, the finite element space, spanned by the basis functions $\{N_i\}_{i=1}^M$. The solutions $\mathbf{F}_n \in V_M$ of

$$a(\mathbf{W}, \mathbf{F}_n) = \lambda_n (\mathbf{W}, \mathbf{F}_n)_0 \quad \forall \mathbf{W} \in V_M \tag{22}$$

are approximations to the general solutions of (20), converging to $\hat{\mathbf{F}}_n$ as $M \to \infty$.

As $a(.,.)$ and $(.,.)_0$ in (20) are both bilinear forms, their arguments may expressed in terms of the basis functions $\{N_j\}_{j=1}^M$,

$$\mathbf{F}_n = \sum_{j=1}^M c_{nj} N_j, \tag{23}$$

leading to

$$\sum_{j=1}^M a(N_i, N_j) c_{nj} = \lambda_n \sum_{j=1}^M (N_i, N_j)_0 c_{nj} \quad \forall N_i \in V_M. \tag{24}$$

The basis functions are known and therefore the integrals in (19) can be evaluated, leading to a sparse generalized matrix eigenvalue problem (GEVP)

$$\mathbf{A}\mathbf{c}_n = \lambda_n \mathbf{M}\mathbf{c}_n \tag{25}$$

for the coefficients c_{nj}. The matrix $\mathbf{M}$ is real valued, symmetrical and positive definite. The matrix $\mathbf{A}$ is hermitian and indefinite for the $\mathbf{k} \cdot \mathbf{p}$ 8×8 model. For the $\mathbf{k} \cdot \mathbf{p}$ 4×4 and 6×6 models, the matrix can be made negatively definite using a constant zero-energy shift.

The dimensionality and the $\mathbf{k} \cdot \mathbf{p}$ model for a calculation is stored in the element integrals and coefficient matrices. Therefore major parts of the code remain independent of the problem considered. We use triangles, rectangles and tetrahedrons as the partition of the domain Ω and assume constant material parameters for each element. This assumption allows us to evaluate all integrals in (24) analytically leading to a matrix assembly time that is negligible compared to the time spent for solving the eigenvalue problem of (25).

4.2 Generalized eigenvalue equation

Solving the GEVP of (25) resulting from the envelope equations can be a rather delicate problem. For 4×4 and 6×6 models, the desired eigenvalues are at the upper boundary of the matrix spectra. For the $\mathbf{k} \cdot \mathbf{p}$ 8×8 model, the bound states correspond to interior eigenvalues which are more difficult to determine. As only a few matrix eigenvalues are sought, iterative methods such as the Arnoldi [36] or the Jacobi-Davidson [37] method can be applied. The number of public available software packages that are able to solve such complex-hermitian generalized eigenvalue problems is rather restricted. We currently apply the shift-and-invert mode of the iterative Arnoldi algorithm implemented in ARPACK [38]. Using shift-and-invert, the spectra of the original GEVP problem is transformed to a problem where the largest eigenvalues are targeted:

$$\mathbf{A} \to (\mathbf{A} - \tau\mathbf{M})^{-1}. \tag{26}$$

This reduces the number of required Arnoldi iterations to usually 70–250, depending on the system, at the cost that in each Arnoldi iteration, a linear equation

$$(\mathbf{A} - \tau\mathbf{M})\,\mathbf{x} = \mathbf{b} \tag{27}$$

must be solved for changing $\mathbf{b}$. The linear problem can be solved either using iterative or direct methods. Iterative methods have a low memory consumption, but as the equation system has to be solved several times, a direct factorization of the matrix is recommended, given that enough memory is available. Moreover, we have found that some iterative linear equation solvers fail to converge when the matrix $\mathbf{A}$ is large and indefinite. We currently achieve the best performance for moderately large systems using the direct factorization linear equation solver PARDISO 3.3 [39] where a parallel version of the matrix factorization on shared memory machines is available. For very large 3D simulations, we expand the complex equation system into a real valued of double size and apply an iterative solver using GMRES with an incomplete LU factorization with threshold (ILUT) as preconditioner [40].

4.3 Strain equations

To be consistent, we also solve the strain equations using finite elements. We seek the displacement field $\mathbf{u}(\mathbf{x})$ minimizing the strain energy given by (13). Therefore we use the *Rayleigh-Ritz* approach and express the displacement field in terms of the FE basis function as

$$\mathbf{u}(\mathbf{x}) = \sum_i \bar{\mathbf{u}}_i N_i(\mathbf{x}). \tag{28}$$

Using (12) we insert (28) into the strain energy functional of (13). The variation of the energy with respect to the displacement coefficients $\bar{\mathbf{u}}_i$ leads to the equation

$$\frac{\partial}{\partial \bar{\mathbf{u}}_i} \Pi = 0 \quad \forall \bar{\mathbf{u}}_i \tag{29}$$

for the determination of the displacement coefficients. Again all integrals can be evaluated analytically and a sparse linear equation for the displacement coefficients $\bar{\mathbf{u}}_i$

$$\mathbf{A}\bar{\mathbf{u}} = \mathbf{d} \tag{30}$$

is obtained. The relaxation strain is then calculated from the displacement using (12). Finally the resulting strain field is given by the sum of the calculated relaxation strains and the intrinsic strains.

The boundary conditions for the strain equations depend on the considered system. In general, boundary displacements can either be free floating or kept fixed to a position.
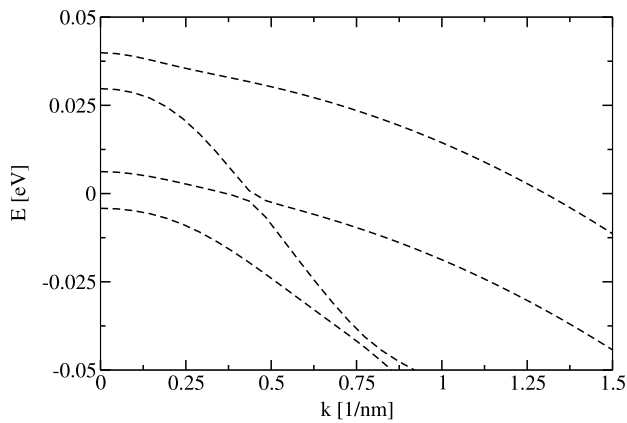
Fig. 2 Valence subbands of a strained 3 nm $In_{0.1}Ga_{0.9}N$ quantum well where the symmetry is broken along the c-axis [0001]

Fig. 3 Valence subbands of a 3 nm $In_{0.1}Ga_{0.9}N$ quantum well where the symmetry is broken along the m-axis [10$\bar{1}$0]. Due to the anisotropy of the crystal, the dispersion is highly dependent on direction of the in-plane wavevector k

5 Applications

In order to demonstrate the capabilities of the solver, we have calculated benchmark examples of different dimensionality. We have chosen a strained nitride quantum well with different orientations, a V-groove GaAs quantum wire and a strained InAs quantum dot as our benchmarks. Interface charges resulting from piezo-electric effects and the change of spontaneous polarization are not included.

5.1 Nitride quantum well

Active regions of blue- and green emitting optoelectronic devices usually consist of multiple nitride quantum wells. In our 1D example, we calculate the band structure for a strained 3 nm $In_{0.1}Ga_{0.9}N/GaN$ quantum well with different orientations using the $\mathbf{k} \cdot \mathbf{p}$ 6×6 model. The quantum well is assumed to be biaxially strained and relaxed in the confinement direction. The dispersion of the c-plane (0001) oriented quantum well is given in Fig. 2. We use the material parameters given in [27] and the operator ordering explained in Sect. 2.2. Figure 3 shows the dispersion of the m-plane (10$\bar{1}$0) quantum well. The m-plane well is modeled by replacing k_x in the Hamiltonian with its operator. The transversal direction is parametrized by the remaining wavenumbers $k_z = k_c$ (along the c-axis) and k_y (in m-plane, orthogonal to c-axis). The resulting dispersion is anisotropic and therefore highly depends on the transversal direction. As the calculations are not memory and time consuming and usually run within a few seconds to minutes, we skip the detailed benchmark analysis of the computational performance.

5.2 V-groove GaAs quantum wire

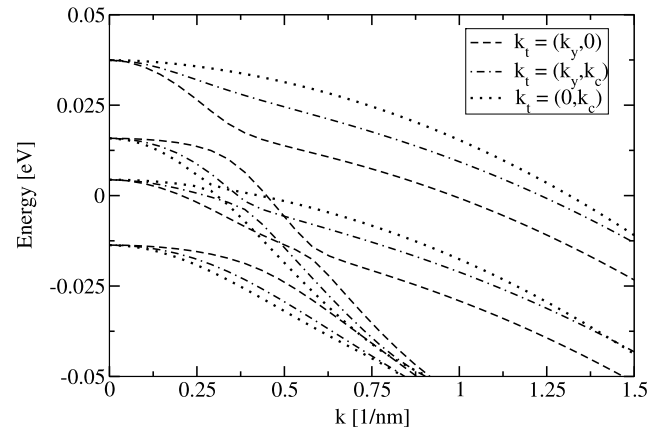The V-groove quantum wire serves as a benchmark structure for complex 2D geometries. The mesh of the model struc-
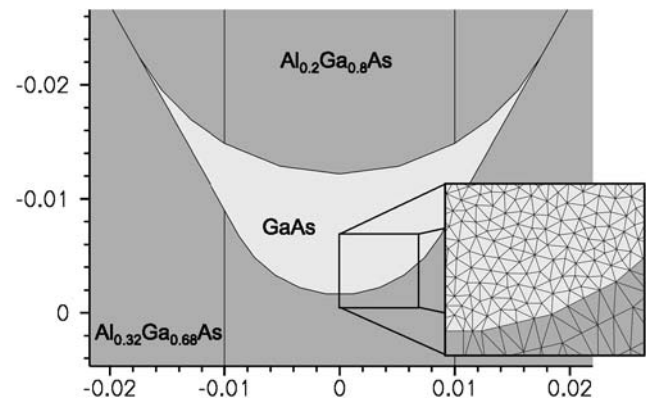

Fig. 4 The benchmark model of a V-groove GaAs quantum wire with triangular meshing. The axes show the length in μm

ture is given in Fig. 4 with units given in μm. The used triangular meshing allows modeling of complex geometrical structures. In the calculation, a mesh using 9570 triangles with a total number of 4901 vertices was applied. The wire is assumed to consist of GaAs embedded in $Al_{0.32}Ga_{0.68}As$ with an $Al_{0.2}Ga_{0.8}As$ quantum well below and on top of the wire. The material parameters were taken from [41]. The alloy parameters were calculated using linear interpolation and bowing. In order to successfully apply the $\mathbf{k} \cdot \mathbf{p}$ 8×8 model, the optical matrix parameters E_p were reduced for all materials (to 21.5 eV, 21.6 eV and 20.5 eV for GaAs, $Al_{0.2}Ga_{0.8}As$ and $Al_{0.32}Ga_{0.68}As$) to keep the equation system elliptic [7]. The resulting conduction band states are given in Fig. 5. The benchmark example was solved for 32 transversal k points and for all implemented $\mathbf{k} \cdot \mathbf{p}$ zincblende models on a workstation equipped with a 2.6 GHz dual-core opteron 1218 processor. All calculations used the direct-factorization solver PARDISO 3.3. The time and memory consumption required for the benchmark examples are listed in Table 1.
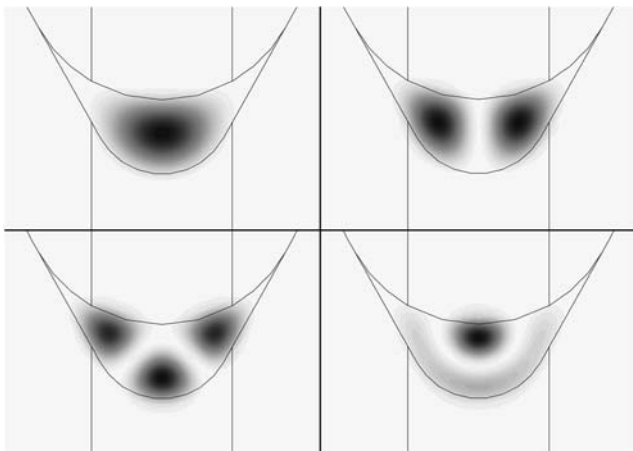
Fig. 5 The probability density of the lowest conduction subband states of the GaAs quantum wire, calculated using $\mathbf{k} \cdot \mathbf{p}$ 8×8

Table 1 Time and memory consumption for the quantum wire benchmark example. The times are given in terms of wallclock seconds. The peak memory column gives the required peak resident memory size

$\mathbf{k} \cdot \mathbf{p}$ Model	Total time	Fact.	Fwd./Bkwd.	Peak mem
4×4	428 [s]	37 [s]	366 [s]	221 MB
6×6	623 [s]	63 [s]	524 [s]	349 MB
8×8	923 [s]	119 [s]	750 [s]	486 MB

The benchmark was performed using two Open MP threads, although the performance increase of the additional thread is minimal. The majority of the time is spent in the forward-/backward substitution process during the Arnoldi iteration which is not parallelized for complex-hermitian matrices in PARDISO 3.3 and therefore represents the current bottleneck regarding performance of tdkp.

5.3 Pyramidal InAs–GaAs quantum dot

The 3D example considered is a pyramidal capped InAs quantum dot embedded within GaAs including a wetting layer (WL) of a few monolayers. The base length of the dot varies between 10.9 and 19.96 nm. Pyramidal quantum dots have been studied extensively in the literature using the selected $\mathbf{k} \cdot \mathbf{p}$ models [13, 14, 18] and finite differences. Here we use a structure similar to [18] to study the solver in terms of speed and memory consumption for very large models. Therefore we use three different meshes with 66'000, 110'000 and 140'000 vertices and calculate the electronic states using $\mathbf{k} \cdot \mathbf{p}$ 4×4 and 8×8 models including strain effects. Each problem is solved using the direct solver PARDISO 3.3 and an iterative GMRES implementation [40]. The iterative solver uses an incomplete LU preconditioner with a threshold of 0.001. The examples were calculated on a shared memory machine with 64 GB memory and four 3 GHz single core opteron 856 processors, ex-
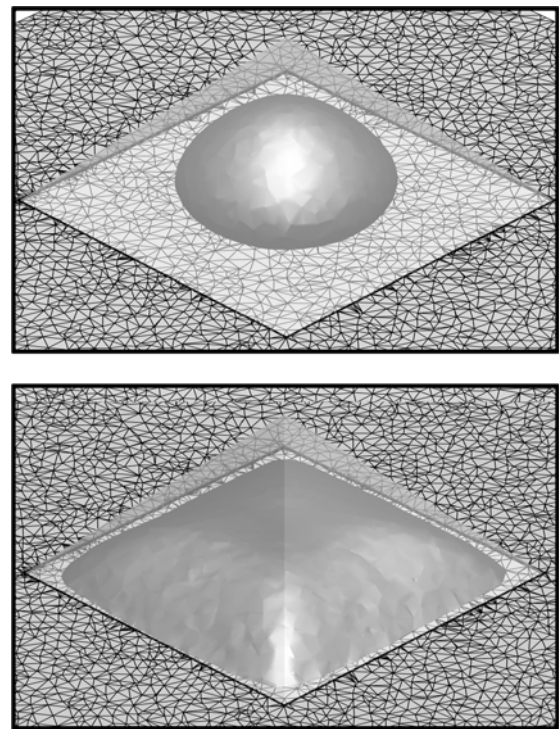

Fig. 6 Iso-probability surface at $|\Psi|^2 = 50\%$ of its peak value for the first conduction- (*upper*) and valence band states in a pyramidal quantum dot of base length 10.9 nm, calculated using $\mathbf{k} \cdot \mathbf{p}$ 8×8 and strain. The mesh of the wetting layer is displayed in the background

cept the $\mathbf{k} \cdot \mathbf{p}$ 8×8 system with 140'000 vertices that was solved on similar machine equipped with 128 GB memory due to the required 71 GB of memory for the direct solver. The parameters were taken from [41] at 6.5 K for the plotted data and at 300 K for the benchmarks. The optical matrix parameter E_p and γ_3 were reduced for the $\mathbf{k} \cdot \mathbf{p}$ 8×8 model to ensure elliptic parameters (E_p: 22.5 eV for GaAs and 21 eV for InAs, γ_3: 2.84 for GaAs). The iso-surfaces for a probability density of $|\Psi|^2 = 50\%$ of the peak value for the first conduction and valence band states are given in Fig. 6. The energies of the first nine bound states with respect to the unstrained GaAs band edges plotted against the base length of the dot are shown in Fig. 7. Compared to [18], we observe a stronger quantization of the states (especially for the first states). The energy of the first conduction band state is 100 meV lower than in [18]. We attribute this to the methodological differences. In [18], the InAs WL is modeled as a graded InGaAs WL reproducing the integral indium amount. In our simulation, the unstructured meshing allows us to exactly reproduce the one monolayer InAs WL with a large number of vertices, leading to an increase of the quantized volume and therefore to more strongly bound states. Furthermore, in contrast to [18], we find the excited electron states to be slightly extending into the WL. Omission of the WL shifts the conduction band states at low base lengths up by 75 meV. However, the $\mathbf{k} \cdot \mathbf{p}$ method is probably
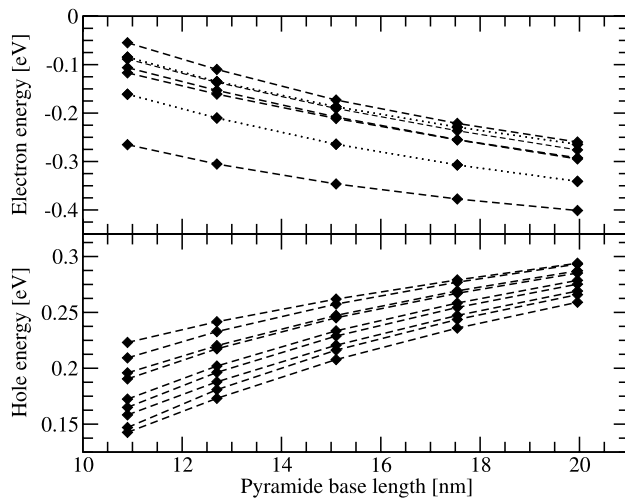
Fig. 7 Energies of the pyramidal quantum dot with respect to the unstrained GaAs band edges of the nine strongest bound electron and hole states. The *x*-axis denotes the base length of the pyramide. The *dotted lines* represent doubly degenerate states
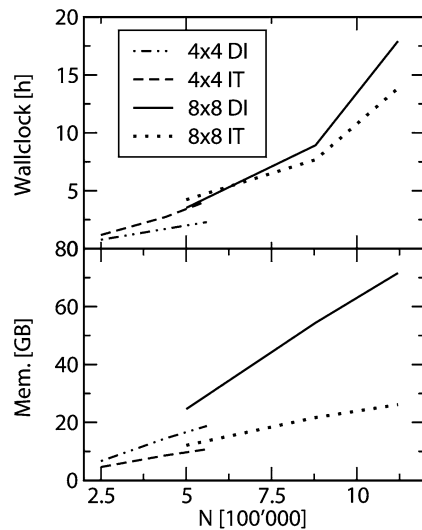

Fig. 8 Benchmark results for the unstrained 3D pyramidal quantum dot. The results were obtained using a four-node server equipped with 3.0 GHz Opteron 856 processors. The *x*-axis denotes the matrix size N (degrees of freedom). The *upper figure* shows the required wallclock time versus matrix size for **k·p** 4×4 (*black*) and 8×8 (*grey*) using direct (DI, *dashed*) and iterative solver (IT, *dash-dotted*). In the *lower figure*, the peak resident memory size (in GB) is plotted against the matrix size

unsuitable for the modeling of the thin WL, where atomistic effects dominate.

The absence of piezo-electricity in our current implementation further increases the quantization and leads to a higher symmetry of the system. This results in a degeneracy of the second and third (and eight and ninth) conduction band states, displayed by the dotted lines in Fig. 7.

Benchmark results for the unstrained 3D pyramidal quantum dot of base length 13.6 nm are plotted in Fig. 8. The

resulting matrix size is plotted against the required peak resident memory (lower figure) and wallclock time (in hours, upper figure). An interesting observation is the linear memory consumption with matrix size for both solvers, although the direct solver requires approximately twice as much memory compared to the iterative solver. PARDISO 3.3 is faster for the smaller problems while for the larger problems, the iterative solver needs less time. This observation is related to the fact that all relevant parts of the iterative solver code are properly parallelized while PARDISO 3.3 runs on a single thread during forward- and backward substitution.

6 Conclusions

The basic result of our work is a consistent finite element derivation and implementation of the **k·p** envelope equations that is applicable directly to the band structure of quantum wells, wires and dots. Using Burt-Foreman operator ordering and ensuring the ellipticity of the equation system, we are able to reliably calculate spurious solution free subband structures for all standard **k·p** models of zinc-blende and wurtzite materials. The implemented solver is designed to be extensible, efficient and general, and will be particularly useful for the study of transport and luminescence in optoelectronic devices with complex quantized structures of different dimensionalities [42]. The application of the finite element method to the intrinsic strain problem allows us to consistently incorporate strain effects on the electronic properties up to second order and therefore leads to a more complete description of essential physics in these devices.

References

1. Foreman, B.A.: First-principles envelope-function theory for lattice-matched semiconductor heterostructures. Phys. Rev. B **72**, 165,345 (2005)
2. Foreman, B.A.: Valence-band mixing in first-principles envelope-function theory. Phys. Rev. B **76**, 045,327 (2007)
3. Wang, L.W., Williamson, A.J., Zunger, A., Jiang, H., Singh, J.: Comparison of the **k · p** and direct diagonalization approaches to the electronic structure of inas/gaas quantum dots. Appl. Phys. Lett. **76**, 339 (2000)
4. Wood, D.M., Zunger, A.: Successes and failures of the **k · p** method: A direct assessment for gaas/alas quantum structures. Phys. Rev. B **53**, 7949 (1996)
5. Fu, H., Wang, L.W., Zunger, A.: Applicability of the **k · p** method to the electronic structure of quantum dots. Phys. Rev. B **57**, 9971 (1998)
6. Zunger, A.: On the farsightedness (hyperopia) of the standard **k · p** model. Phys. Stat. Sol. (A) **190**, 467 (2002)

7. Veprek, R.G., Steiger, S., Witzigmann, B.: Ellipticity and the spurious solution problem of $\mathbf{k} \cdot \mathbf{p}$ envelope equations. Phys. Rev. B **76**, 165,320 (2007)

8. Burt, M.G.: The justification for applying the effective-mass approximation to microstructures. J. Phys.: Condens. Matter **4**, 6651–6690 (1992)

9. Burt, M.G.: Fundamentals of envelope function theory for electronic states and photonic modes in nanostructures. J. Phys.: Condens. Matter **11**, R53–R83 (1999)

10. Foreman, B.A.: Elimination of spurious solutions from eight-band $\mathbf{k} \cdot \mathbf{p}$ theory. Phys. Rev. B **56**, R12,748 (1997)

11. Trellakis, A., Zibold, T., Andlauer, T., Briner, S., Smith, R.K., Morschl, R., Vogl, P.: The 3d nanometer device project nextnano: Concepts, methods, results. J. Comput. Electron **5**, 285–289 (2006)

12. Pryor, C., Pistol, M.E., Samuelson, L.: Electronic structure of strained inp/$Ga_{0.51}In_{0.49}$P quantum dots. Phys. Rev. B **56**, 10,404 (1997)

13. Pryor, C.: Eight-band calculations of strained inas/gaas quantum dots compared with one-, four-, and six-band approximations. Phys. Rev. B **57**, 7190 (1998)

14. Pryor, C.: Geometry and material parameter dependence of inas/gaas quantum dot electronic structure. Phys. Rev. B **60**, 2869 (1999)

15. Holm, M., Pistol, M.E., Pryor, C.: Calculations of the electronic structure of strained inas quantum dots in inp. J. Appl. Phys. **92**, 932 (2002)

16. Schuurmans, M.F.H., t'Hooft, G.W.: Simple calculations of confinemenet states in a quantum well. Phys. Rev. B. **31**, 8041 (1985)

17. Stier, O., Bimberg, D.: Modeling of strained quantum wires using eight-band $\mathbf{k} \cdot \mathbf{p}$ theory. Phys. Rev. B **55**, 7726 (1997)

18. Stier, O., Grundmann, M., Bimberg, D.: Electronic and optical properties of strained quantum dots modeled by 8-band $\mathbf{k} \cdot \mathbf{p}$ theory. Phys. Rev. B **59**, 5688 (1999)

19. Chuang, S.L., Physics of Optoelectronic Devices. Wiley, New York (1995)

20. Pidgeon, C.R., Brown, R.N.: Interband magneto-absorption and Faraday rotation in insb. Phys. Rev. **146**, 146 (1966)

21. Enders, P., Barwolff, A., Woerner, M., Suisky, D.: $\mathbf{k} \cdot \mathbf{p}$ theory of energy bands, wave functions, and optical selection rules in strained tetrahedral semiconductors. Phys. Rev. B **51**, 16,695 (1995)

22. Lassen, B., Voon, L.C.L.Y., Willatzen, M., Melnik, R.: Exact envelope-function theory versus symmetrized hamiltonian for quantum wires: a comparison. Solid State Commun. **132**, 141 (2004)

23. Chuang, S.L., Chang, C.S.: $\mathbf{k} \cdot \mathbf{p}$ method for strained wurtzite semiconductors. Phys. Rev. B **54**, 2491 (1996)

24. Hader, J., Moloney, J.V., Thranhardt, A., Koch, S.W.: Nitride Semiconductor Devices: Principles and Simulation, chap. Interband Transitions in InGaN Quantum Wells, pp. 145–167. USA, NUSOD Institute Newark (2007), DE 19714-7204

25. Mireles, F., Ulloa, S.E.: Ordered hamiltonian and matching conditions for heterojunctions with wurtzite symmetry: Gan/Al_xGa_{1-x}N quantum wells. Phys. Rev. B **60**, 13,659 (1999)

26. Mireles, F., Ulloa, S.E.: Strain and crystallographic orientation effects on the valence subbands of wurtzite quantum wells. Phys. Rev. B. **62**, 2562 (2000)

27. Vurgaftman, I., Meyer, J.R.: Band parameters for nitrogen-containing semiconductors. Appl. Phys. Rev. **94**, 3675 (2003)

28. Braess, D.: Finite Elemente. Springer, Berlin (1997)

29. Pryor, C., Kim, J., Wang, L.W., Williamson, A.J., Zunger, A.: Comparison of two methods for describing the strain profiles in quantum dots. J. Appl. Phys. **83**, 2548 (1998)

30. Bir, G.L., Pikus, G.E.: Symmetry and Strain-Induced Effects in Semiconductors. Wiley, New York (1974)

31. Bahder, T.B.: Eight-band $\mathbf{k} \cdot \mathbf{p}$ model of strained zinc-blende crystals. Phys. Rev. B **41**, 11,992 (1990)

32. Ram-Mohan, L.R.: Finite Element and Boundary Element Applications in Quantum Mechanics. Oxford University Press, Oxford (2002)

33. Johnson, H.T., Freund, L.B.: The influence of strain on confined electronic states in semiconductor quantum structures. Int. J. Sol. Struct. **38**, 1045 (2001)

34. Park, S.H., Ahn, D., Lee, Y.T.: Finite element analysis of valence band structures in quantum wires. J. Appl. Phys. **96**, 2055 (2004)

35. Schwab, C.: p- and hp- Finite Element Methods. Clarendon, Oxford (1998)

36. Sorensen, D.C.: Implicitly restarted Arnoldi/Lanczos methods for large scale eigenvalue calculations. Tech. Rep. TR-96-40 (1996). http:citeseer.ist.psu.edu/174335.html

37. Sleijpen, G.L.G., Van der Vorst, H.A.: A Jacobi-Davidson iteration method for linear eigenvalue problems. SIAM J. Matrix Analysis Appl. **17**(2), 401–425 (1996). http:citeseer.ist.psu.edu/sleijpen00jacobidavidson.html

38. Lehoucq, R.B., Sorensen, D.C., Yang, C.: Arpack Users Quide: Solution of Large Scale Eigenvalue Problems by Implicitly Restarted Arnoldi Methods. SIAM, Philadelphia (1998)

39. Schenk, O., Gärtner, K.: Solving unsymmetric sparse systems of linear equations with pardiso. J. Future Gener. Comput. Syst. **20**, 475–487 (2004)

40. Röllin, S.: Parallel iterative solvers in computational electronics. Ph.D. thesis, ETH Zürich (2004)

41. Vurgaftman, I., Meyer, J.R.: Band parameters for iii-v compound semiconductors and their alloys. Appl. Phys. Rev. **89**, 5815 (2001)

42. Steiger, S., Veprek, R.G., Witzigmann, B.: Unified simulation of transport and luminescence in optoelectronic nanostructures. J. Comput. Electron. (2008, this issue). doi:10.1007/s10825-008-0261-z